UC Riverside
UC Riverside Previously Published Works

Title

Optothermal generation, trapping, and manipulation of microbubbles.

Permalink

Journal

Optics Express, 28(12)

ISSN

1094-4087

Authors

Sarabia-Alonso, JA
Ortega-Mendoza, JG
Ramírez-San-Juan, JC
et al.

Publication Date

2020-06-08

DOI

10.1364/oe.389980

Peer reviewed

Optothermal generation, trapping, and manipulation of microbubbles

J. A. SARABIA-ALONSO,[1] J. G. ORTEGA-MENDOZA,[2] J. C. RAMÍREZ-SAN-JUAN,[1] P. ZACA-MORÁN,[3] J. RAMÍREZ-RAMÍREZ,[1] A. PADILLA-VIVANCO,[2] F. M. MUÑOZ-PÉREZ,[2] AND R. RAMOS-GARCÍA[1],*

[1]*Departamento de Óptica, Instituto Nacional de Astrofísica, Óptica y Electrónica, Luis Enrique Erro # 1, Puebla 72840, Mexico*
[2]*División de Posgrado, Universidad Politécnica de Tulancingo, Ingenierías # 100, 43629 Tulancingo, Mexico*
[3]*Instituto de Ciencias, Benemérita Universidad Autónoma de Puebla, Ecocampus Valsequillo, 72960 Puebla, Mexico*
*rgarcia@inaoep.mx

Abstract: The most common approach to optically generate and manipulate bubbles in liquids involves temperature gradients induced by CW lasers. In this work, we present a method to accomplish both the generation of microbubbles and their 3D manipulation in ethanol through optothermal forces. These forces are triggered by light absorption from a nanosecond pulsed laser ($\lambda = 532$ nm) at silver nanoparticles photodeposited at the distal end of a multimode optical fiber. Light absorbed from each laser pulse quickly heats up the silver-ethanol interface beyond the ethanol critical-point (~ 243 °C) before the heat diffuses through the liquid. Therefore, the liquid achieves a metastable state and owing to spontaneous nucleation converted to a vapor bubble attached to the optical fiber. The bubble grows with semi-spherical shape producing a counterjet in the final stage of the collapse. This jet reaches the hot nanoparticles vaporizing almost immediately and ejecting a microbubble. This microbubble-generation mechanism takes place with every laser pulse (10 kHz repetition rate) leading to the generation of a microbubbles stream. The microbubbles' velocities decrease as they move away from the optical fiber and eventually coalesce forming a larger bubble. The larger bubble is attracted to the optical fiber by the Marangoni force once it reaches a critical size while being continuously fed with each bubble of the microbubbles stream. The balance of the optothermal forces owing to the laser-pulse drives the 3D manipulation of the main bubble. A complete characterization of the trapping conditions is provided in this paper.

1. Introduction

Bubbles play a key role in fields such as thermodynamics [1,2], microfluidics [3–5], biomedical [6,7], hydraulics [8,9] but is also relevant in applications such as valves [10,11], motors [8,12], needle-free injectors [7], optical trapping and sorting [11,13–15] among others. These applications require extreme spatial control of bubbles' position to accomplish their purposes; however, this is quite difficult to achieve because many dynamic processes are involved. A great deal of both experimental and theoretical works have been carried out to fully understand the dynamics of the bubbles allowing their 2D manipulation based on acoustic, thermal, and optical phenomena [16–20]. The combination of these last two, also called optothermal effect, has shown to have several advantages at the microscale regime [21,22]. On one hand, optical phenomena provide both noncontact and noninvasive approaches of bubbles manipulation while thermal phenomena can provide forces many orders of magnitude larger than optical ones [16,19,23]. So optothermal phenomena offers the best of the two worlds.

Optical generation of microbubbles in liquids is typically achieved by laser radiation with either CW [16–19] or pulsed lasers [24–26]. The former one needs an absorbent medium to convert the incident light into heat [22,27,28], whereas the latter one occurs in highly transparent media through means of multiphoton absorption leading to optical breakdown [29–31]. Optical manipulation of microbubbles is not an easy task since the refractive index of vapor is smaller than the surrounding liquid; however, "bottle" beams, i.e., donuts-shape beams with a dark center allows manipulation of low refractive index particles [32–34]. Optical trapping of large bubbles cannot be achieved with optical means; however, recently it was reported an optothermal method [18] for the generation and 2D manipulation of microbubbles by Marangoni force [16-20].

In this work, we present both experimental and theoretical results of 3D manipulation of microbubbles generated by light-absorption from a nanosecond pulsed laser at silver nanoparticles (AgNPs) photodeposited onto the core of a multimode optical fiber. Each laser-pulse generates a small bubble by the explosive phase transition, which later ejects microbubbles into the liquid, forming a microbubbles-stream that moves away from the tip of the optical fiber until they coalesce, forming a large microbubble. This bubble is eventually attracted to the optical fiber by the Marangoni force while it is continuously hit and fed by the microbubbles-stream. The balance of the involved forces drives the 3D manipulation of the large bubble. To our best knowledge, this is the first time that quasi-stable 3D trapping and manipulation of bubbles is reported.

2. Experimental section

In our experimental setup, a nanosecond laser pulse (Spectra Physics Q-Switch at 532 nm, τ_p=5 ns & 10 kHz repetition rate) is coupled to a multimode optical fiber (50 μm core diameter) by a 10x microscope objective (MO). At the distal end of the optical fiber, AgNPs (Sigma-Aldrich, particle size < 100 nm) were photodeposited following the procedure reported in [35,36] until 3.5 dB of attenuation was achieved. After that, the fiber end with the photodeposited nanoparticles was submerged vertically (*z*-axis) in a glass cuvette containing pure ethanol. For visualization of the bubble dynamics, a 50x microscope objective (Mitutoyo, NA = 0.26) is coupled to a high-speed camera Phantom v7.3. A halogen lamp, as depicted in Fig. 1, supplies the illumination.
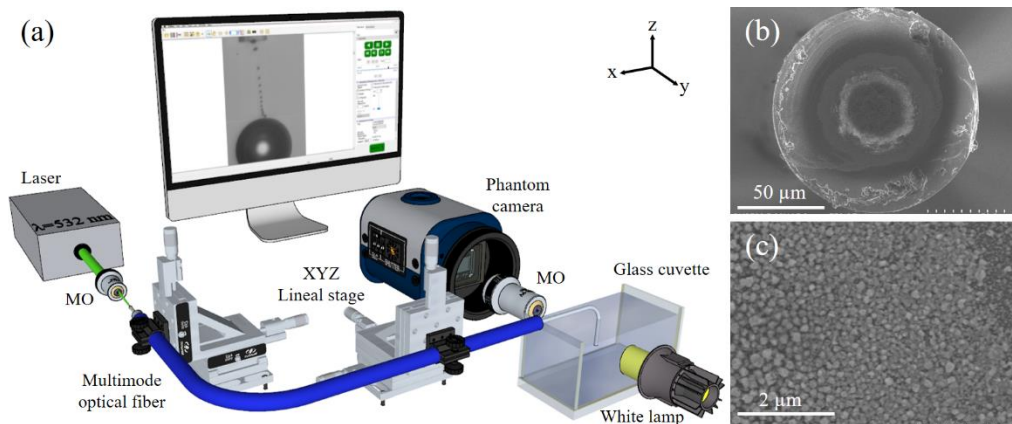

Fig. 1. (a) Experimental setup for the generation and 3D manipulation of microbubbles. A pulsed laser is coupled to the multimode optical fiber using a microscope objective (MO). Bubbles dynamics are viewed with a fast Phantom camera. (b) Image of the distal end of the multimode optical fiber obtained with a SEM after 3.5 dB of attenuation was achieved. (c) Closer view of the optical fiber core showed on (b).

It is important to clarify that no bubbles are produced when no nanoparticles are photodeposited at the energy levels reported in this work. So the driving mechanism of microbubble generation is thermal effects produced by light absorption at the nanoparticles.

3. Experimental results

Figure 2(a) shows snapshots of the bubble growth dynamics using 2.1 μJ per pulse laser energy. With each laser pulse, a bubble is detached from the fiber end forming a long column of bubbles with an increasing diameter (and decreasing velocity) as they move away. A similar phenomenon was reported by Ohl *et al.* [37,38], but they employed a CW laser source or Joule heating. Besides, they do not report the formation of a larger bubble or its trapping and manipulation. As the bubbles speed decreases, they catch up and eventually coalesce forming a larger bubble, called hereafter, as the main-bubble (125 μm of radius after $t \sim 1.6$ s). According to our experimental results, it was noticed that the main-bubble approaches the fiber end (heat source) as it grows. In fact, it can be trapped and manipulated in 3D as shown in Visualization 1. Figure 2(b) shows the time dependence of the main-bubble radius measured from the video and the calculated one by adding the ejected small bubbles with an average radius of 5.5 μm. The growth rate of the main-bubble is faster at the beginning because the contribution of each small bubble to the volume of the main one is significant but eventually, its contribution becomes less significant for such reason the dynamics of the radius of the main-bubble is better described as with a double exponential function, $r(t) = r_{max}[1 - r_1 exp(-t/t_1) - r_2 exp(-t/t_2)]$, where r_{max} is the maximum bubble radius, r_1, r_2, t_1, and t_2 are radius and time constant of the fast and slow contribution to the bubble growth, respectively (see Fig. 2 for its values). The disagreement between both curves is because the coalescent bubble radius is larger at the beginning of the video but as the main-bubble is attracted towards the fiber the coalescent bubbles become smaller, i.e., the radii of the coalescent bubbles are spatially and temporarily varying, however, our approaches gives a good estimate of the final main-bubble radius. It is important to notice that for >13 000 bubbles, its radius does not change appreciably, and thus quasi-stable trapping and manipulation can be achieved.
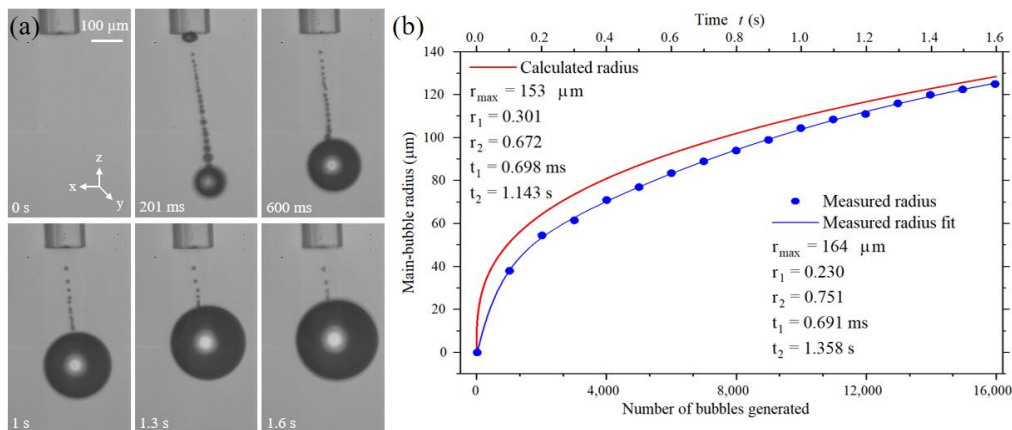

Fig. 2. Growth of the main-bubble as a function of time. (a) Snapshots of the temporal evolution of the main-bubble radius recorded at 6,600 fps. (b) Blue dots correspond to the measured from the video main-bubble radius. The continuous blue line is fit to a double exponential function. The lower horizontal axis represents the number of coalesced bubbles and the upper one the corresponding elapsed time. The red solid line indicates the calculated radius of the main-bubble as a function of microbubbles generated at 2.1 μJ per pulse-energy at a repetition rate of 10 kHz.
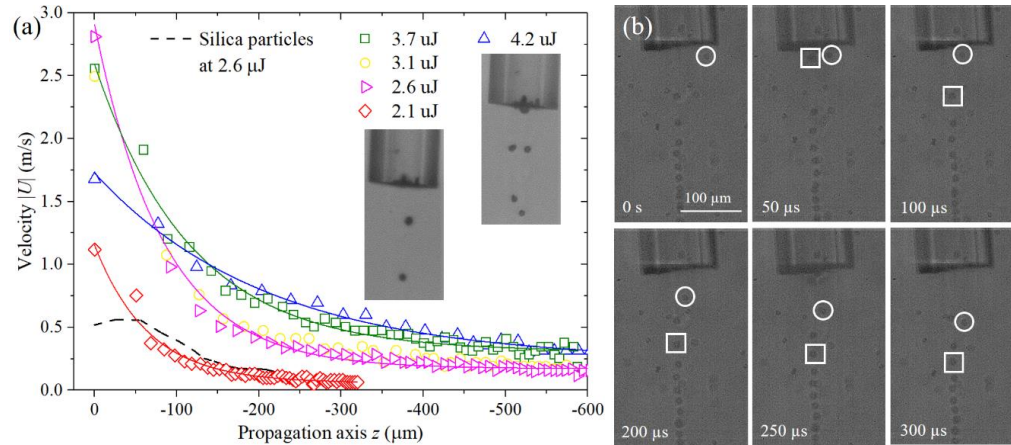
Fig. 3. (a) Profile of the bubble's velocity as a function of the laser energy, extracted from recorded images at 43,000 fps. Continuous lines are fit to an exponential function. (b) Snapshot of the tracers and bubbles when a 2.6 μJ of laser energy was used. White circles and white squares indicate the tracer and bubble displacement, respectively. Both the bubble and the tracer start from the same position at t = 50 μs, however, the bubble moves faster as time goes on.

Figure 3(a) shows the velocity U of the ejected bubbles from the tip of the optical fiber along the light propagation (z-axis) at different laser pulse's energy. The bubbles' velocity was extracted from the recorded video at 43,000 fps using the Phantom control camera software. The frame rate provides information of the temporal dynamics while the spatial information was obtained from the diameter (125 μm) of the optical fiber. In all cases, the velocity of the ejected bubbles
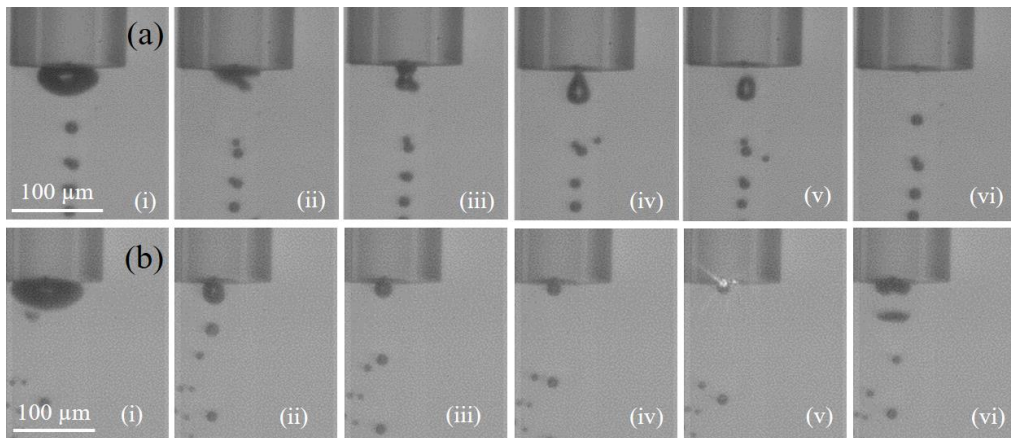
Fig. 4. (a) Snapshot of the optothermal generation of microbubbles: (i) maximum bubble size, (ii) bubble collapse, (iii) bubble ejection, (iv-vi) bubble moves away from the optical fiber. (b) 4.2 μJ of laser-pulse energy. (i) Maximum cavitation bubble. (ii-iv) Temporal evolution of the remaining bubble. (v) Bright spots represent scatter laser-light due to AgNPs picked up by the video-camera. (vi) Bubble ejection due to the counterjet. The frame rate in all cases was 43,000 fps.

is faster around the fiber end and then decreases exponentially with the distance. As the laser energy increases, the velocity also increases. For pulse energy < 2 μJ no bubbles were formed and for pulse energy > 4.2 μJ, two bubbles were expelled but with lower velocity, as it is shown in the inset of Fig. 3(a). The thermal gradient produced by the nanoparticles at the fiber end also produces convective currents. In order to measure the velocity of the convective currents, silica microparticles (3 μm) were added as tracers to the solution and by video-analysis, its velocity (velocity$_{max}$ ~0.5 m/s) was determined (broken line). The microparticles tracers stops around 300 μm and then they are dragged out of the field of view by the convective currents. Figure 3(b) is a closed-up around the fiber end where a microparticle (enclosed by a circle) is tracked along with a bubble (enclosed by a square). Notice that the bubble velocity is always faster than the tracer one and travel longer along the propagation distance. This distance is determined by the laser pulse energy.

Figure 4(a) shows snapshots of the bubbles' temporal evolution generated with 3.1 μJ per pulse energy, i.e., single bubble generation regime. With each laser pulse, a semi-spherical shape bubble is created that rapidly grows up to its maximal radius R_{max} while remains attached to the fiber, this is the typical behavior of thermocavitation bubbles [39,40]. After that, the bubble collapses taking a mushroom-shape form and a small bubble is expelled from the fiber end. However, if the pulse energy is increased beyond 4.2 μJ, as shown in Fig. 4(b), the bubble is larger, and its collapse is more complex since two or even three bubbles are created, and a smaller bubble always remains on the fiber. Detailed time evolution of the bubble dynamics was not possible with our fast camera, so only snapshots were captured.

4. Discussion

As pointed out above, no bubbles were produced in the absence of nanoparticles on the fiber end, so the driving mechanism of bubble generation is of thermal origins produced by light absorption at the nanoparticles. Heat is transfer to ethanol from the irradiated zone due to diffusion. The diffusion time is given by [41]: $\tau_{diff} = d^2/4D_t$, where d is the thickness of the absorbing medium and D_t is the thermal diffusivity (171.92×10^{-6} m^2/s for silver [42] and 85.19×10^{-9} m^2/s for ethanol [43]). For silver nanoparticles and a thickness of $d = 100$ nm, τ_{diff} ~ *15 ps*, which means that within the pulse the films radiate efficiently but ethanol is a bad radiator, so its temperature will increase. It is crucial to determine the temperature increase at the AgNPs-ethanol interface; however, it is quite difficult to perform a direct measure because to our best knowledge, there is no thermal sensor capable of operating at the times scales involved ($\tau_p < 10$ ns) in a small heated volume. However, let us take some reasonable assumptions to numerically (COMSOL Multiphysics) estimate both the temperature-induced and its spatial distribution. First, the incident laser pulse has a Gaussian profile and the photodeposited film is assumed to be a homogenous thin-film of constant thickness. The generated heat per unit volume is calculated as $Q = \alpha I$, where α is the absorption coefficient (7.2086×10^6 m^{-1} for silver [42] and 6.8×10^{-2} m^{-1} for ethanol [44]) and I is the optical intensity of the Gaussian beam defined as $I = (2E/\pi\tau_p w_0^2) \exp(-2r^2/w_0^2) \exp(-t^2/\tau_p^2)$ where E is the pulse energy, τ_p is the pulse duration and w_0 is the optical fiber core radius. The ethanol's absorption coefficient is very small in comparison to the silver one; therefore, the silver film is the only heat source. Figure 5 shows the temperature profile induced by a single laser pulse at the AgNPs-ethanol interface at different laser pulse's energy. The energy pulses correspond to the ones used on the experiment. In all cases, the temperature rises quickly beyond the ethanol boiling point [45] $T_b = 78.24$ °C without boiling and reaching the thermodynamic critical temperature of ethanol [45] $T_c = 243$°C, i.e., the temperature of the film is so hot that a vapor film is created between film and the liquid limiting further increase on vaporization. Beyond this metastable state, ethanol undergoes an explosive phase transition to vapor, producing a fast-expanding bubble (not included in our simulation). Once the vapor phase is achieved no further heating of the ethanol is possible

due to the well-known boiling crisis [46]. On the other hand, once the laser pulse is off, the temperature slowly decreases $T(t) = T_0 + \Delta T exp(-t/\tau_0)$ where T_0 is the ambient temperature, ΔT is the maximum temperature reached by the pulse and τ_0 is characteristic time (~ 55 ns). When the next pulse arrives, 100 µs later, time the film has reached a steady-state temperature, and the whole process repeat again. Thus, with each laser pulse a bubble is produced, and a train of bubbles are expelled from the fiber end. It is important to mention that no phase transition was included in our simulation, so the actual liquid temperature could not be determined.
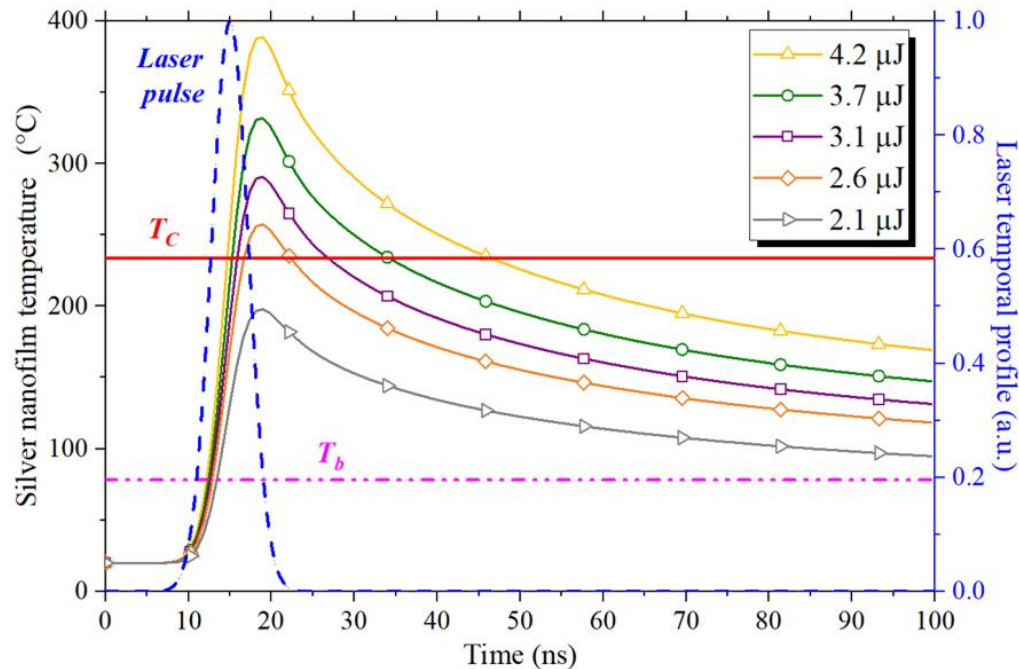
Fig. 5. Temperature profile at the AgNPs-ethanol interface obtained by solving the heat diffusion equation coupled to the Navier-Stokes equations using COMSOL Multiphysics. The phase explosion is more likely to occur around Tc ~243 °C (continuous red line). The temperature increase at the interface is a linear function of the laser energy. Color solid lines represent the temporal profile of the temperature at the AgNPs-ethanol interface due to light absorption. The blue broken line represents the temporal profile of one laser pulse. The pink double-dot line represents the pure ethanol boiling temperature Tb ~ 78 °C.

The generation of the column of bubbles just described here was also recently reported using CW lasers and electrical microheaters [37,38]. In their studies, they heat (optically or electrically) a homogenous metallic thin-film and observed rising bubbles at a very high repetition rate ~100 kHz. Upon heating, the liquid in contact with the metallic film is explosively evaporated and after some transient regime, a stable bubble generation is observed. It is well known that a cavitation bubble collapsing near a solid substrate will produce a counterjet explained by the non-spherical collapse theory developed by Rattray [47–49]. Before the collapse, the semi-spherical bubble takes toroidal shape due to the formation of a counterjet directed towards the substrate. In the case of heated substrates, the counterjet hits the film and is immediately vaporized producing a secondary bubble while the vapor film keeps attached to the fiber end and this process repeats with each laser pulse. However, in Ref. [37,38] they neither observe the coalescence nor the trapping of bubbles (probably they occurred outside the field of view), given the smaller bubbles ($R \sim 2$ µm) and the velocity at which the bubbles are expelled.

In our experiments, we could not observe details of the bubble dynamics because of the limited temporal resolution of our camera. The bubble lifetime τ_r in close proximity to a substrate [26,49,50] is given by [47]:

$$\tau_r \approx \tau_c(1 + 0.205\gamma), \tag{1}$$

where $\gamma = H/R_{max}$ is standoff parameter, H is the distance between the wall and the center of the bubble, R_{max} is the maximal semi-spherical radius, and τ_c is the collapse time for a spherical bubble, also called the Rayleigh collapse time [51], given by:

$$\tau_c \approx 0.915\sqrt{\frac{\rho_l}{P_\infty - P_v}}R_{max}, \tag{2}$$

where $\rho_l = 789$ kg/m^3 is liquid ethanol density [45], $P_\infty = 101.33$ kPa and $P_v = 7.87$ kPa are the pressure in the liquid [52] away from the bubble ($P_\infty = P_{atm}$), and the vapor pressure of ethanol [52], respectively. According to Eq. (1), the non-spherical collapse time for the bubbles reported here is $\tau_r \sim 6$ μs, which is smaller than the temporal resolution of our video-camera, $\tau_{frame} \sim 23$ μs. This explains why we cannot record both the counterjet and the bubble collapse dynamics.

As shown in Fig. 3(a), the bubbles are expelled from the optical fiber reaching velocities of up to 2.5 m/s, much larger compared to those reported in Ref. [37,38], and then decrease as they move away from the AgNPs-ethanol interface and eventually they coalesce at a certain distance along the propagation axis producing a larger bubble, which is eventually trapped when it reaches a critical size. An estimate of the critical size is not an easy task, but we can estimate the quasi-steady-state trapping by analyzing the forces involved in its trapping. Two of them are of thermal origin produced by light absorption on the nanoparticles: the Marangoni force and drag force due to convective currents. There are two additional forces: one due to the momentum's transfer to the main-bubble by the continuous coalescence of bubbles and buoyancy force. A bubble immersed into a temperature gradient, as the one produced by the nanoparticles on the fiber end, will suffer a tangential stress on its wall owing to the temperature dependence of the surface tension; the bubble will move towards the heat source while the liquid flows to the colder regions, this is called Marangoni force $\overrightarrow{F_M}$ or thermocapillary force [18–20], which is given by:

$$\overrightarrow{F_M} = -2\pi R^2 \nabla T \frac{d\sigma}{dT}, \tag{3}$$

where R is the microbubble radius, ∇T is the temperature gradient in the propagation axis and $d\sigma/dT$ is the temperature derivative of ethanol surface tension σ (-0.1 × 10^{-3} Nm^{-1}K^{-1}). The drag force [35] due to the convective currents can be written as $\overrightarrow{F_d} = 6\pi\mu RU$. The column of bubbles moves in opposite direction to the main-bubble, as it shows in Fig. 2(a). So, the main-bubble suffers an impact from the bubbles-stream, called inertia force [53–55] $\overrightarrow{F_i} = ma = \frac{4}{3}\pi R^3 \rho_l C_b \frac{dU}{dt}$, where $C_b = 1/2$ is the bubble-shape coefficient [54]. In addition, once the bubble is created the buoyancy and gravity force appear. These forces are given by [21] $\overrightarrow{F_b} = \frac{4}{3}\pi\rho_l gR^3$ and $\overrightarrow{F_g} = \frac{4}{3}\rho_v gR^3$, respectively, where g is the gravitational acceleration, U is the microbubble velocity, $\mu = 1.17 \times 10^{-3}$ Pa·s is the dynamic ethanol viscosity [45], $\rho_v = 1.43$ kg/m^3 is the vapor ethanol density [45]. However, since the liquid density is two orders of magnitude greater than the vapor density, gravity force will be neglected. On the other hand, since the vapor refractive index (~ 1) is smaller than the liquid one, the bubble will be pushed away from the beam. Actually, given the large size of the beam and optical power, the gradient optical force [35] in this case is five orders smaller than both the drag and buoyancy force [23,34]. The radiation pressure is also negligible small since only the beam leaving the fiber rapidly diffracts [35], so all optical forces are negligibly small and will not be taken into account in the following analysis. In addition, since Marangoni force scale $\sim R^2$, this means that only the large bubble will be

under the effect of this force, for example, a bubble of $R = 5\,\mu m$ near the fiber end will experience $\overrightarrow{F_M} \sim 20$ nN while large bubbles of $R > 100\,\mu m$ will experience a force > 400 times larger. Small bubbles cannot be attracted towards the fiber end since the drag force for small bubbles is larger. For example, using the velocity data for small bubbles [Fig. 3(a)] moving away from the fiber we calculated drag force $\overrightarrow{F_d} \sim 190$ nN, i.e., the drag force is almost 20 times larger than the Marangoni force for the small bubbles. On the other hand, a bubble of $R = 125\,\mu m$ close to the fiber end will feel $\overrightarrow{F_M} \sim 15\,\mu N$ and $\overrightarrow{F_d} \sim 0.190\,\mu N$; therefore, the bubble will be attracted to the fiber end.

Hence, the total force $\overrightarrow{F_T}$ acting over the main-bubble moving in the propagation axis $\pm z$ used in this study is:

$$\overrightarrow{F_T} = \overrightarrow{F_b} \pm \overrightarrow{F_M} \mp \overrightarrow{F_d} \mp \overrightarrow{F_i}, \tag{4}$$

where the $\pm$ sign indicates the direction of light propagation along $\pm z$, as sketched in Fig. 6(a). Figure 6(b) shows the total force over a main-bubble of $R = 131\,\mu m$ versus the distance along the z-axis. When the total force is equal to zero, the bubble will stop, so, $\overrightarrow{F_M} + \overrightarrow{F_b} = \overrightarrow{F_d} + \overrightarrow{F_i}$. Thus, the main-bubble will reach a theoretical quasi-steady-state at $z_{crit} = -439.7\,\mu m$, as it is shown in Fig. 6(b) inset. Notice that the dominant force near to the fiber is the Marangoni one, but the other forces become important, as the main bubble is farther away. If the laser is continuously on, the bubble will continue growing until it touches the fiber and eventually leaves the fiber due to buoyancy force.
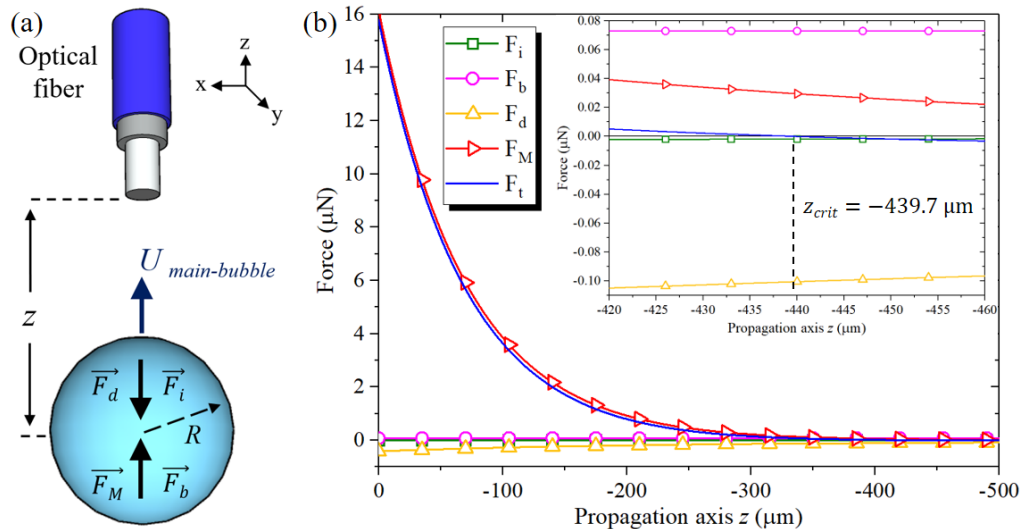
Fig. 6. (a) Free-body diagram of the forces involved in the main-bubble manipulation. (b) Total force over a main-bubble of R = 131 µm illuminated with pulses of 3.7 µJ of energy as a function of the propagation axis.

Figure 7(a) shows snapshots of a main-bubble of radius $R = 131\,\mu m$ approaching the optical fiber illuminated with pulses of 3.7 µJ of energy. The complete temporal evolution of the main-bubble radius is not shown because it occurred out of the field of view, nevertheless, one can observe the main-bubble displacement in $+z$ direction while the bubbles-stream moves along the $-z$ direction; quasi-steady-state trapping of the main-bubble trapped occurs at $z_{exp} = -437.8\,\mu m$. However, this position is continuously changing since the main-bubble is continuously growing, as it is shown in Fig. 7(b). In this figure, the theoretical-quasi-steady-state is obtained from the

total force around the equilibrium position. Although, the rate of change of the bubble is not negligible $\sim 30\,\mu m/s$, as it is shown in Fig. 2(b). The quasi-steady trapping can be maintained from microseconds to milliseconds, as it is shown in Visualization 1. In fact, for the case of Fig. 7(b) a change in the bubble ratio of 3 µm (occurs in 100 ms) it means a change of $\sim 30\,\mu m$ in the trapping distance or just above 5% variations. The bubble can be trapped around 20 seconds (as it is shown in Visualization 1), but it continuously approaches the fiber and eventually leaves the trap since the buoyancy force dominates over all others forces. Nevertheless, these results give us the confidence to predict the trapping distance as a function of pulse-energy and to achieve quasi-steady-state 3D trapping.
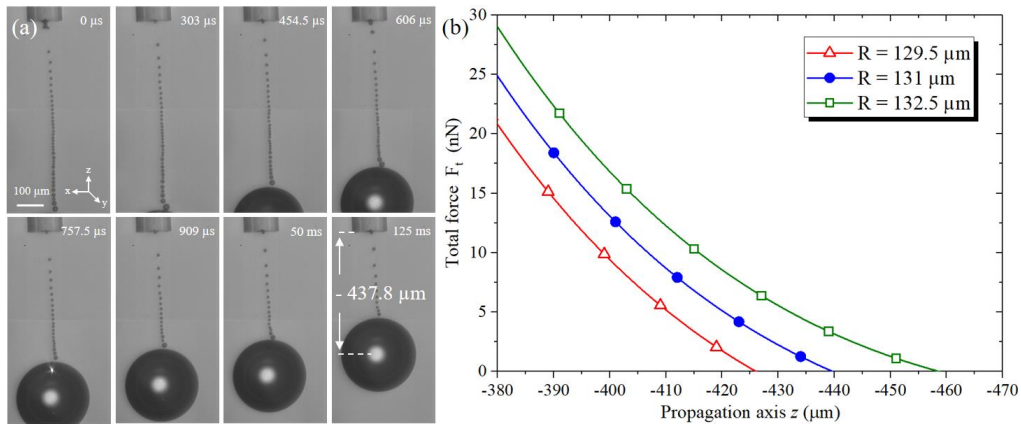
Fig. 7. Spatial displacement of the main-bubble Visualization 2. (a) The main-bubble moves in + z direction whereas the bubbles-stream does it in -z direction. (b) Total force over a main-bubble around the quasi-steady-state trapping distance for bubbles of different radii. Total force over a bubble of 129.5 µm of radius (red triangles), 131 µm of radius (blue dots) and 132.5 µm of radius (green squares) obtaining quasi-steady-state trapping at -430.2 µm, -439.7 µm and -451.4µm, respectively.

5. Conclusions

In summary, it was shown both theoretically and experimentally the quasi-steady-state 3D manipulation of vapor bubbles using a nanosecond pulsed laser. Light absorption at silver nanoparticles (AgNPs) photodeposited onto the core of a multimode optical fiber heats the liquid beyond its boiling point. Each laser-pulse generates a small bubble (attached to the fiber end) by the explosive phase transition, which later ejects microbubbles into the liquid, forming a microbubbles-stream that moves away from the tip of the optical fiber until they coalesce, forming a large microbubble. We have shown that those bubbles coalesce at certain distance z, generating a large bubble that grows with each coalescence. This bubble is eventually attracted to the optical fiber by the Marangoni force while it is continuously hit and fed by the microbubbles stream. The balance of the involved forces drives the 3D manipulation of the large bubble. To our best knowledge, this is the first time that both quasi-stable 3D trapping and manipulation of large bubbles are reported.

Funding

Disclosures

The authors declare no conflicts of interest.

References

1. E. Lukianova-Hleb, Y. Hu, L. Latterini, L. Tarpani, S. Lee, R. A. Drezek, J. H. Hafner, and D. O. Lapotko, "Plasmonic Nanobubbles as Transient Vapor Nanobubbles Generated around Plasmonic Nanoparticles," ACS Nano **4**(4), 2109–2123 (2010).
2. D. A. Boyd, J. R. Adleman, D. G. Goodwin, and D. Psaltis, "Chemical Separations by Bubble-Assisted Interphase Mass-Transfer," Anal. Chem. **80**(7), 2452–2456 (2008).
3. G. M Whitesides, "The origins and the future of microfluidics," Nature **442**(7101), 368–373 (2006).
4. D. Ahmed, X. Mao, B. K. Juluri, and T. J. Huang, "A fast microfluidic mixer based on acoustically driven sidewall-trapped microbubbles," Microfluid. Nanofluid. **7**(5), 727–731 (2009).
5. T. H. Wu, Y. Chen, S. Y. Park, J. Hong, T. Teslaa, J. F. Zhong, D. D. Carlo, M. A. Teitelll, and P. Y. Chiou, "Pulsed laser triggered high speed microfluidic fluorescence activated cell sorter," Lab Chip **12**(7), 1378–1383 (2012).
6. L. A. Hardy, J. D. Kennedy, C. R. Wilson, P. B. Irby, and N. M. Fried, "Analysis of thulium fiber laser induced bubble dynamics for ablation of kidney stones," J. Biophotonics **10**(10), 1240–1249 (2017).
7. C. Berrospe, C. W. Visser, S. Schlautmann, D. F. Rivas, and R. Ramos-García, "Toward jet injection by continuous-wave laser cavitation," J. Biomed. Opt. **22**(10), 105003 (2017).
8. J. Kao, X. Wang, J. Warren, J. Xu, and D. Attinger, "A bubble-powered micro-rotor: conception, manufacturing, assembly and characterization," J. Micromech. Microeng. **17**(12), 2454–2460 (2007).
9. A. Hashmi, G. Yu, M. Reilly-Collette, G. Heiman, and J. Xu, "Oscillating bubbles: a versatile tool for lab on a chip applications," Lab Chip **12**(21), 4216–4227 (2012).
10. K. Khoshmanesh, A. Almansouri, H. Alboushi, P. Yi, R. Soffe, and K. Kalantar-Zadeh, "A multi-functional bubble-based microfluidic system," Sci. Rep. **5**(1), 9942 (2015).
11. P. Rogers and A. Neild, "Selective particle trapping using an oscillating microbubble," Lab Chip **11**(21), 3710–3715 (2011).
12. Q. Y. You, H. J. Zhang, Y. D. Wang, and J. J. Chen, "Dynamic properties of symmetric optothermal microactuator," J. Micromech. Microeng. **27**(10), 105011 (2017).
13. S. K. Chung, K. Rhee, and S. K. Cho, "Bubble actuation by electrowetting-on-dielectric (EWOD) and its applications: A review," Int. J. Precis. Eng. Manuf. **11**(6), 991–1006 (2010).
14. L. Lin, X. Peng, Z. Mao, W. Li, M. N. Yogeesh, B. B. Rajeeva, E. P. Perillo, A. K. Dunn, D. Akinwande, and Y. Zheng, "Bubble-pen lithography," Nano Lett. **16**(1), 701–708 (2016).
15. S. Fujii, K. Kanaizuka, S. Toyabe, K. Kobayashi, E. Muneyuki, and M.-a. Haga, "Fabrication and placement of a ring structure of nanoparticles by a laser-induced micronanobubble on a gold surface," Langmuir **27**(14), 8605–8610 (2011).
16. O. V. Angelsky, A. Y. Berkshaev, P. P. Maksimyak, A. P. Maksimyak, and S. G. Hanson, "Low-temperature laser-stimulated controllable generation of micro-bubbles in a water suspension of absorptive colloid particles," Opt. Express **26**(11), 13995–14009 (2018).
17. O. V. Angelsky, A. Y. Berkshaev, P. P. Maksimyak, A. P. Maksimyak, S. G. Hanson, and S. M. Kontush, "Controllable generation and manipulation of micro-bubbles in water with absorptive colloid particles by CW laser radiation," Opt. Express **25**(5), 5232–5243 (2017).
18. J. G. Ortega-Mendoza, J. A. Sarabia-Alonso, P. Zaca-Morán, A. Padilla-Vivanco, C. Toxqui-Quitl, I. Rivas-Cambero, J. Ramirez-Ramirez, S. A. Torres-Hurtado, and R. Ramos-García, "Marangoni force-driven manipulation of photothermally-induced microbubbles," Opt. Express **26**(6), 6653–6662 (2018).
19. A. Miniewicz, C. Quintard, H. Orlikowska, and S. Bartkiewicz, "On the origin of the driving force in the Marangoni propelled gas bubble trapping mechanism," Phys. Chem. Chem. Phys. **19**(28), 18695–18703 (2017).
20. J. I. Ramos, "Lumped models of gas bubbles in thermal gradients," Appl. Math. Model. **21**(6), 371–386 (1997).
21. Y. Xie and C. Zhao, "An optothermally generated surface bubble and its applications," Nanoscale **9**(20), 6622–6631 (2017).
22. G. Baffou, J. Polleux, H. Rigneault, and S. Monneret, "Super-Heating and Micro-Bubble Generation around Plasmonic Nanoparticles under cw Illumination," J. Phys. Chem. C **118**(9), 4890–4898 (2014).
23. H. Takahira, M. Shirasawa, and S. Yamasaki, "Laser Manipulation of Bubbles and Evaluation of Its Optical Force," JSME Int. J., Ser. B **43**(3), 393–399 (2000).
24. D. Faccio, G. Tamošauskas, E. Rubino, J. Darginavičius, D. G. Papazoglou, S. Tzortzakis, A. Couairon, and A. Dubietis, "Cavitation dynamics and directional microbubble ejection induced by intense femtosecond laser pulses in liquids," Phys. Rev. E **86**(3), 036304 (2012).
25. A. Siems, S. A. Weber, J. Boneberg, and A. Plech, "Thermodynamics of nanosecond nanobubble formation at laser-excited metal nanoparticles," New J. Phys. **13**(4), 043018 (2011).
26. O. Supponen, D. Obreschkow, P. Kobel, M. Tinguely, N. Dorsaz, and M. Farhat, "Shock waves from nonspherical cavitation bubbles," Phys. Rev. Fluids **2**(9), 093601 (2017).
27. R. Pimentel-Domínguez, J. Hernández-Cordero, and R. Zenit, "Microbubble generation using fiber optic tips coated with nanoparticles," Opt. Express **20**(8), 8732–8740 (2012).

28. M. Kitz, S. Preisser, A. Wetterwald, M. Jaeger, G. N. Thalmann, and M. Frenz, "Vapor bubble generation around gold nano-particles and its application to damaging of cells," Biomed. Opt. Express **2**(2), 291–304 (2011).

29. A. Vogel, J. Noack, K. Nahen, D. Theisen, S. Busch, U. Parlitz, D. X. Hammer, G. D. Noojin, B. A. Rockwell, and R. Birngruber, "Energy balance of optical breakdown in water at nanosecond to femtosecond time scales," Appl. Phys. B **68**(2), 271–280 (1999).

30. A. Vogel, S. Busch, and U. Parlitz, "Shock wave emission and cavitation bubble generation by picosecond and nanosecond optical breakdown in water," J. Acoust. Soc. Am. **100**(1), 148–165 (1996).

31. A. Vogel, N. Linz, S. Freidank, and G. Paltauf, "Femtosecond-Laser-Induced Nanocavitation in Water: Implications for Optical Breakdown Threshold and Cell Surgery," Phys. Rev. Lett. **100**(3), 038102 (2008).

32. W. Hu, K. S. Ishii, and T. A. Ohta, "Micro-assembly using optically controlled bubble microrobots," Appl. Phys. Lett. **99**(9), 094103 (2011).

33. P. Y. Chiou, A. T. Ohta, and M. C. Wu, "Massively parallel manipulation of single cells and microparticles using optical images," Nature **436**(7049), 370–372 (2005).

34. P. H. Jones, E. Stride, and N. Saffari, "Trapping and manipulation of microscopic bubbles with a scanning optical tweezer," Appl. Phys. Lett. **89**(8), 081113 (2006).

35. J. G. Ortega-Mendoza, F. Chávez, P. Zaca-Morán, C. Felipe, G. F. Pérez-Sánchez, G. Beltran-Pérez, O. Goiz, and R. Ramos-García, "Selective photodeposition of zinc nanoparticles on the core of a single-mode optical fiber," Opt. Express **21**(5), 6509–6518 (2013).

36. P. Zaca-Morán, E. Kuzin, J. Torres-Turiján, J. G. Ortega-Mendoza, F. Chávez, G. F. Pérez-Sánchez, and L. C. Gómez-Pavón, "High gain pulsed erbium-doped fiber amplifier for the nonlinear characterization of SWCNTs photodeposited on optical fibers," Opt. Laser Technol. **52**, 15–20 (2013).

37. F. Li, R. Gonzalez-Avila, D. M. Nguyen, and C. D. Ohl, "Oscillate boiling from microheaters," Phys. Rev. Fluids **2**(1), 014007 (2017).

38. D. M. Nguyen, L. Hu, J. Miao, and C. D. Ohl, "Oscillate Boiling from Electrical Microheaters," Phys. Rev. Appl. **10**(4), 044064 (2018).

39. J. C. Ramirez-San-Juan, E. Rodriguez-Aboytes, A. E. Martinez-Canton, O. Baldovino-Pantaleon, A. Robledo-Martinez, N. Korneev, and R. Ramos-García, "Time-resolved analysis of cavitation induced by CW lasers in absorbing liquids," Opt. Express **18**(9), 8735–8742 (2010).

40. J. P. Padilla-Martinez, C. Berrospe-Rodriguez, G. Aguilar, J. C. Ramirez-San-Juan, and R. Ramos-García, "Optic cavitation with CW lasers: A Review," Phys. Fluids **26**(12), 122007 (2014).

41. J. H. Lienhard IV and J. H. Lienhard V, *A heat transfer textbook* (Phlogiston Press, 2017).

42. J. Wang and M. Fiebig, "Measurement of the thermal diffusivity of aqueous solutions of alcohols by a laser-induced thermal grating technique," Int. J. Thermophys. **16**(6), 1353–1361 (1995).

43. Y. Jiang, S. Pillai, and M. A. Green, "Re-evaluation of literature values of silver optical constants," Opt. Express **23**(3), 2133–2144 (2015).

44. H. Cabrera, J. Akbar, D. Korte, I. Ashraf, E. E. Ramírez-Miquet, E. Marín, and J. Niemela, "Absorption Spectra of Ethanol and Water Using a Photothermal Lens Spectrophotometer," Appl. Spectrosc. **72**(7), 1069–1073 (2018).

45. L. E. John, "Ethanol," in *Encyclopedia of Chemical Technology*, Kirk-Othmer, ed. (Wiley, 2004).

46. P. Lloveras, F. Salvat-Pujol, L. Truskinovsky, and E. Vives, "Boiling crisis as a critical phenomenon," Phys. Rev. Lett. **108**(21), 215701 (2012).

47. R. Maurice Jr., *Pertubation effects in cavitation bubble dynamics* (California Institute of Technology, 1951).

48. C. R. Bruce, *Nonspherical vapor bubble collapse* (California Institute of Technology, 1970).

49. E. Johnsen and T. Colonius, "Numerical simulations of non-spherical bubble collapse," J. Fluid Mech. **629**, 231–262 (2009).

50. O. Lindau and W. Lauterborn, "Cinematographic observation of the collapse and rebound of a laser-produced cavitation bubble near a wall," J. Fluid Mech. **479**, 327–348 (2003).

51. C. E. Brennen, *Cavitation and Bubble Dynamics* (Oxford University, Inc., 1995).

52. W. M. Haynes, *CRC Handbook of Chemistry and Physics* (CRC Press, 2017).

53. C. Lazarus, A. N. Pouliopoulos, M. Tinguely, V. Garbin, and J. J. Choi, "Clustering dynamics of microbubbles exposed to low-pressure 1-MHz ultrasound," J. Acoust. Soc. Am. **142**(5), 3135–3146 (2017).

54. C. D. Ohl, A. Tijink, and A. Prosperetti, "The added mass of an expanding bubble," J. Fluid Mech. **482**, 271–290 (2003).

55. E. Klaseboer, R. Manica, M. H. W. Hendrix, C. D. Ohl, and D. Y. C. Chan, "A force balance model for the motion, impact, and bounce of bubbles," Phys. Fluids **26**(9), 092101 (2014).